Vat polymerization additive manufacturing of thermite charges for satellite demise applications (T4D)

Oscar Pratola[1], Stefania Carlotti[2], Jacopo Domaschio[3], Alessandro Finazzi[4], Filippo Maggi*

[1] Politecnico di Milano, Italy - MSc. Student; oscar.pratola@mail.polimi.it
[2] Politecnico di Milano, Italy - Assistant Professor; stefania.carlotti@polimi.it
[3] Politecnico di Milano, Italy - PhD Student; jacopo.domaschio@polimi.it
[4] Politecnico di Milano, Italy - Post-doctoral Research Assistant; alessandro.finazzi@polimi.it
[*] Corresponding Author: Politecnico di Milano, Italy - Full professor; filippo.maggi@polimi.it

Abstract

Thermites are versatile energetic materials. In most cases, they consist of an oxide and a metal producing a spontaneous reaction between. They are characterized by high energy density and elevated reaction temperatures. Recently, the use of thermites is under exploration as an option to assist the demise of satellites during their reentry after decommissioning. The concept consists of supporting the destruction of space platforms by locating energetic charges on board, through small thermite-based components introduced in key points. Production of said components is under investigation through a photocurable resin loaded with Mg/SiO_2 thermite powder and shaped through DLP printing. As a proof of concept, cylindrical test charges have been produced, reaching a mass loading of up to 60 % by mass of thermite. Actual loading and onset temperature of the thermitic reaction were analyzed through thermogravimetry and differential thermal analysis. In most of the cases, samples showed an almost nominal loading with a maximum shift below 2 % and good uniformity within the height. The onset of the thermitic reaction was consistent in all the samples.

Keywords: thermite-for-demise, 3D printing, UV curing, magnesium, silicon dioxide

---

1 Introduction

In recent years, the number of spacecraft in LEO* has increased and, powered by an always growing space economy (AA.VV. 2024), it is predicted to maintain this exponential trend in the future. The progressive crowding of space is leading to more and more stringent regulations over the years to enforce early demise and mitigate orbit saturation. Three of the major milestones in this sense are: the 25-years rule, the 5-years rule, and, more recently, the voluntary best-in-class practices reported in ESA's Zero Debris Charter (AA.VV. 2023, 2025). According to ESA's ESSB-ST-U-007 (AA.VV. 2023), design-for-demise (D4D) is the preferred method to control casualty risk of reentering space platform after the end of their operative life. ESA's Annual Space Environment Report showed a change in the type of launched objects. In the past, the numbers of launched objects were smaller and the mass of a single spacecraft was either very large (more than 1000 kg) or small (less than 100 kg). Most of today's market is characterized by private telecommunication contractors requiring payloads in the range between 100 kg to 1000 kg. This is critical for space debris since, for every reentering object larger than 200 kg, about 10 % to 40 % of its initial mass survives the atmospheric ablation reaching the ground (Waswa and Hoffman 2012). Survivability is

*LEO: Low Earth Orbit (160 km to 2000 km altitude) difficult to predict and depends on several details such as initial mass, type of materials, shapes, initial orbit, and satellite configuration. According to regulations, the predicted on-ground casualty risk shall remain below the threshold value of 10^{-4} (AA.VV. 2025). The value cumulates the effect of each *k-th* fragment reaching the ground with kinetic energy higher than 15 J, and it is proportional to the casualty area $A_{C,k}$ (see eq. (1)) of the *k-th* piece of debris (AA.VV. 2023).

$$A_{C,k} = \left(\sqrt{A_{i,k}} + \sqrt{A_h}\right)^2 \tag{1}$$

In the formula, $A_{i,k}$ is the cross section area of the *k-th* fragment, and A_h is the human cross section area, conventionally set to $0.36\,\mathrm{m}^2$. For this reason, mastering the section and the residual kinetic energy of fragments surviving the atmospheric phase of an orbital reentry allows the implementation of correct demise strategies.

Critical elements of the spacecraft, such as titanium propellant tanks, reaction wheels, optical payloads, and balancing masses, are generally hard to dismantle and, frequently, they can reach the ground (Finazzi et al. 2024c; Lips 2025; Seiler and Smet 2020). Moreover, in case of failed controlled reentry, dangerous debris might fall on inhabited areas. This occurrence recently happened with a Falcon 9 reportedly failing the reentry of the orbital stage over the ocean, and causing large debris (mainly tanks) to fall on the European continent (Foust 2025).

D4D is an engineering method that aims at controlling the fragmentation of a reentering space platform with specific design choices. Among the others, maximizing the available heat represents an option (Cattani et al. 2021) and it can be implemented through the thermite-for-demise (T4D) concept.

T4D provides an onboard source of extra enthalpy consisting of a pyrotechnic charge of thermite that can be triggered by either an igniter or by the re-entry heat flux itself, passively. Most of thermites are energetic materials composed of metal and metal oxide, which undergo a redox reaction, developing heat. By thoughtfully choosing the right thermite ingredients and using methods like mechanical activation to fine-tune the ignition temperature, the chance of accidental heat-triggered reactions over the platform's working life can be minimized, while reliable ignition during reentry is possible. This result was proven by both the work of Monogarov and by the SPADEXO[†] test campaign, exposing material samples under simulated re-entry conditions (Finazzi et al. 2024a; Monogarov et al. 2020). The SPADEXO campaign also showed drawbacks in the use of loose thermite powder. First of all, the gas flow can entrain the particulate, removing it from the target areas. Moreover, dust of energetic materials can lead to serious safety issues during handling, due to leakage and sensitivity, or contamination of spacecraft apparatuses. For these reasons the use of compressed thermites was first proposed, but preliminary iterations showed high brittleness of the samples, calling for another and stabler compaction method (Finazzi et al. 2024a,b,c).

This study proposes the use of polymer binders, increasing powder cohesion and avoiding powder leakage issue. More specifically, Digital Light Processing (DLP) printing is utilized to shape thermite charges through ultra-violet (UV) curing. This industrial technology is commonly used in 3D printing devices, it is accessible with low prices, and potentially enables the production of shapes with high geometrical complexity.

[†] **SPADEXO:** Spacecraft Demise During Re-entry Expedited Using Various Exothermic Reactions

In the following, the outcomes of the preliminary testing of this technology are discussed. Section 2.1 presents the main aspects of resin printing technology and the pivotal parameters to account for. Section 2.2 explains how the materials used in resin production (Section 2.3) were selected. Subsequently, the printing process is described in Section 2.4 and the results are presented in Section 3.

2 Materials and Methods

2.1 DLP Printing Technology

Additive manufacturing is an enabling technology that permits to achieve highly complex geometry for no additional cost, compared to traditional subtractive manufacturing (Kanishka and Acherjee 2023). Among various printing technologies, binder jetting and DLP printing are among the most suitable for the use of resins loaded with powders. The latter was preferred here, since DLP printers are commercially available and relatively inexpensive, making this technology particularly suitable for a preliminary test campaign on a laboratory scale.

In a DLP 3D printer, the building platform is lowered inside of the vat containing photopolymer resin. A UV light source is located beneath the vat. An LCD screen is placed between the resin and the source and lets the UV irradiate part of the resin at the bottom of the tank, changing pixels opacity. The process is controlled by the electronic board according to a used-defined slicing program. One resin layer at a time is cured. As the stage raises carrying the cured layer attached to it, a small amount of new uncured resin naturally flows within the vat and covers the layer that was just formed and cured. The full 3D shape is built by stacking up layer-by-layer.

In this work, the Anycubic Mono X2 printer was used together with a custom-made reduced vat and building plate, to reduce the amount of materials required for each print. The manufacturer does not declare the working wavelength of their printer, thus it was assumed to be around 405 nm since it is widely used by other comparable machines (Anonymous 2025). The UV radiation at this wavelength provides a curing energy of 3.05 eV (computed via Planck's equation). This value is of primary importance relative to the band gaps of the particles, as explored below in Section 2.2.

2.2 Material Selection

2.2.1 Requirements Definition

The first of the three main aspects to be considered in the material selection is the band gap. It represents the minimum energy required to excite an electron from the valence band to the conduction band. When the incident radiation energy exceeds the band gap, electrons are promoted to the conduction band, absorbing energy. Consequently, the radiation available for the curing process is reduced compromising the efficiency of the process.

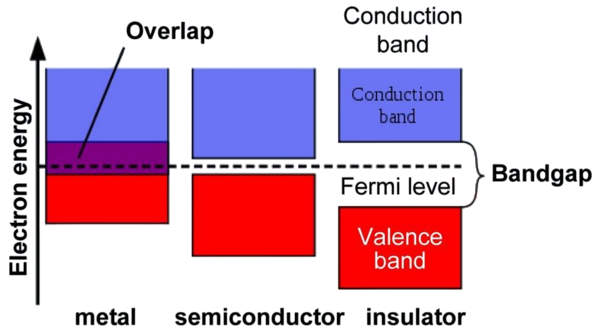

Figure 1: Band gap in metals, semiconductors and insulators

As illustrated in Figure 1, metals exhibit overlapping valence and conduction bands, requiring no additional energy for electron promotion. In thermites, composites of metals and metal oxides, only the oxide components are significantly affected by band gap considerations. Oxides optimal for photocuring present band gap greater than irradiating energy (Gao et al. 2024).

Another key requirement for powder selection is particle size. Particles can induce light scattering, which deviates incident radiation and may cure unintended areas, thereby reducing the geometrical accuracy of the printed part (McClain et al. 2020). Moreover, particle diameter and shape affect viscosity, as smaller or irregular particles may increase the viscosity of the powder-resin slurry (Mueller et al. 2010). A low-viscosity resin can be used to challenge viscosity buildup with filler loading, restoring flowability.

2.2.2 Thermite

The Mg/SiO_2 thermite composition was selected for preliminary testing due to the wide band gap of silica (7 eV), which exceeds the 3.05 eV photocuring threshold (Strehlow and Cook 1973). Moreover, both powders are available in micrometric size, thereby minimizing light scattering effects. The properties of the selected powders are summarized in Table 1.

Table 1: Powder characteristics. Particle sizes were measured using a Malvern Mastersizer 2000 with Scirocco accessory.

Powder	Manufacturer	Purity	Characteristics	Density, g/cm^3
Mg	Thermo Scientific	99.8 %	-325 mesh (measured $D(0.5)$ = 36.628 µm)	1.738
SiO_2	Thermo Scientific	99.0 %	-325 mesh (measured $D(0.5)$ = 1.730 µm)	2.648

The Mg/SiO_2 thermite in stoichiometric ratios (52.2 % by mass of Mg and 47.8 % by mass of SiO_2) undergoes the redox reaction presented in eq. (2), producing an adiabatic flame temperature T_{flame} = 2122.72 K, and releasing 3300.5 J/g of heat of reaction (Fischer and Grubelich 1998; Strehlow and Cook 1973).

$$2\,Mg + SiO_2 \longrightarrow 2\,MgO + Si \tag{2}$$

2.3 Resin Production

Selection of the suspending medium follows a criterion of viscosity minimization to ease the production process. As a reference, the online catalog of Anycubic[‡], the manufacturer of the 3D printer, was considered as a reference. For convenience, a list of available resins for UV printing, with relevant properties, is reported Table 2. In the table, the High Speed 2.0 resin presenting the lowest viscosity, ranging 75 mPa s to 85 mPa s. For this reason, this polymeric matrix was selected in this study. From the chemical viewpoint, the resin is a mixture of acrylates and metacrylates, and it is sensitive to UV curing.

Table 2: Resin Properties and Print Parameters for Anycubic Mono X2 Printer

Resin	Viscosity [mPa · s]	Density [g/cm^3]	Bottom Exp. Time [s]	Normal Exp. Time [s]
Standard Resin	200–230	1.13	25	2.5
ABS-Like Pro V2	300–400	1.1–1.2	20	2.5
High Clear Resin	266	1.05–1.25	25	4
High Speed 2.0	75–85	1.14	18	2–5

A procedure to embed Mg/SiO_2 thermite in the resin was developed. Silica powder was treated with BYK-111 dispersant mixed with acetone and stirred with a magnetic anchor. After one hour of mixing the powder was extracted and moved into a drying oven for 24 h. Magnesium powder was not treated with the mentioned procedure since preliminary tests demonstrated to be ineffective, as shown in Figure 2. Once the drying process was completed for powders, the magnesium and silica powder were added progressively to the resin under vigorous mechanical mixing ($\sim$ 700 $\div$ 1000 RPM). Finally, air was removed from the mixture with an ultrasound mixer for 10 minutes. Initial printing tests demonstrated that magnesium

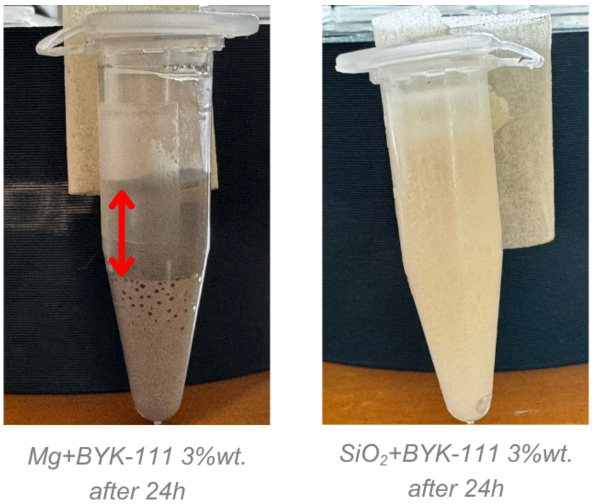

Figure 2: Sedimentation test of magnesium and silica treated with BYK-111 dispersant (after 24 hours). Magnesium (l.h.s) presents a clear phase separation (red arrow), indicating ineffectiveness of the dispersant.

[‡] www.anycubic.com

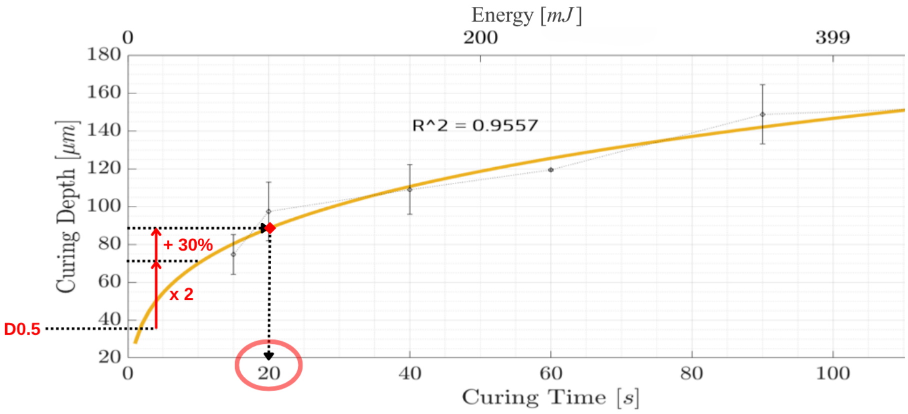

Figure 3: Working curve for Anycubic High Speed Resin loaded with 60 % Mg/SiO_2

interacted with the resin, triggering uncontrolled cross-linking. A coating was applied to the powders, using the same proportions presented by Guo et al. 2008. In general, resins with thermite loads[§] up to 60 % were prepared and the respective working curves were established. Data were than interpolated. The curve in Figure 3 represents the results for 60 % of load. In general, 3D printing with such loading is reportedly feasible, according to the open literature (Smirnov et al. 2022).

2.4 Printing

Printing parameters were iteratively consolidated. Curing time and layer thickness was established from the working curve of the resin. An iterative trial-and-error approach was used to determine the build plate velocity that ensures proper adhesion of the sample. Initial successful tests were obtained with 40 % of loading. Further iterations with progressively higher loadings were then performed while keeping the printing parameters constant to ensure comparability. As best practice, the layer thickness was set to be twice the particle size, taking as a reference the D(0.5) of the coarsest powder. This value was then rounded, yielding 70 µm. Subsequently, the curing time was determined as the value required to cure a layer 30 % greater than the layer thickness in order to ensure the crosslinking between successive sheets. Through the working curve of the polymer-thermite mixture, the final curing time resulted in 20 s. As a rule of thumb, exposure time of the bottom layer is 10 times the normal exposure time and, namely, 200 s. Printing parameters obtained after tuning are summarized in Table 3.

3 Results

Batches of resin with 40 %, 50 %, and 60 % loading were printed using the same printing parameters to ensure comparability. Figure 4 shows the geometrical benchmark used to assess printability at each loading level. Subsequently, the tallest cylindrical sample (30 mm) was characterized via thermogravimetric

[§] Loading: Powder filler fraction
[*] Velocity at which the build plate is raised from the bottom of the vat.
[†] Velocity at which the build plate is immersed in the resin tank.

Table 3: DLP Printing Parameters for Anycubic Mono X2 and High Speed 2.0 resin with Mg/SiO_2 powder filler

Parameter	Value	Unit
From working curve		
Layer thickness	70	µm
Normal Layer Exposure	20	s
Bottom Layer Exposure	200	s
From trial and error		
Z-lift speed*	2	mm/s
Z-retraction speed†	3	mm/s

(a) Sampling scheme

(b) Printed item

Figure 4: Geometrical benchmark for DLP printing

analysis (TG) and differential thermal analysis (DTA). Specimens were collected from the top, middle, and bottom sections of the part for analysis[¶]. TG and DTA were performed at a heating rate of 10 K/min in an inert argon atmosphere using an alumina crucible. Output data were analyzed to determine the pyrolysis onset and end temperatures, as well as the onset temperature of the exothermic reaction. The onset points in both TG and DTA were calculated as the intersection of two tangents: one to the initial baseline, and one at the point of maximum derivative, as illustrated in Figure 5.

Table 4 summarizes the results and clearly shows that the pyrolysis onset temperature is consistent across the samples and shared among all the loadings, with a mean onset temperature of 342.4 °C and standard deviation of 12.3 °C. This suggests that the loading moderately influences the pyrolysis process. Notably, as the loading increases, a decrease in the pyrolysis onset temperature and a concurrent increase in the pyrolysis end temperature were observed.

The onset of the exothermic reaction was consistently identified after the end of pyrolysis, indicating that the associated endothermic reactions may have delayed the onset of the exothermic process. In other words, the binder must be fully pyrolyzed before the reaction begins. The onset temperature of the exothermic

¶ "Bottom" refers to the sample collected near the build plate, whereas "top" refers to the sample collected further from it.

* Computed graphically since the software could not properly interpret the data

† Statistics excludes 40 % loading samples because data are unreliable

‡ Based on only two valid measurements

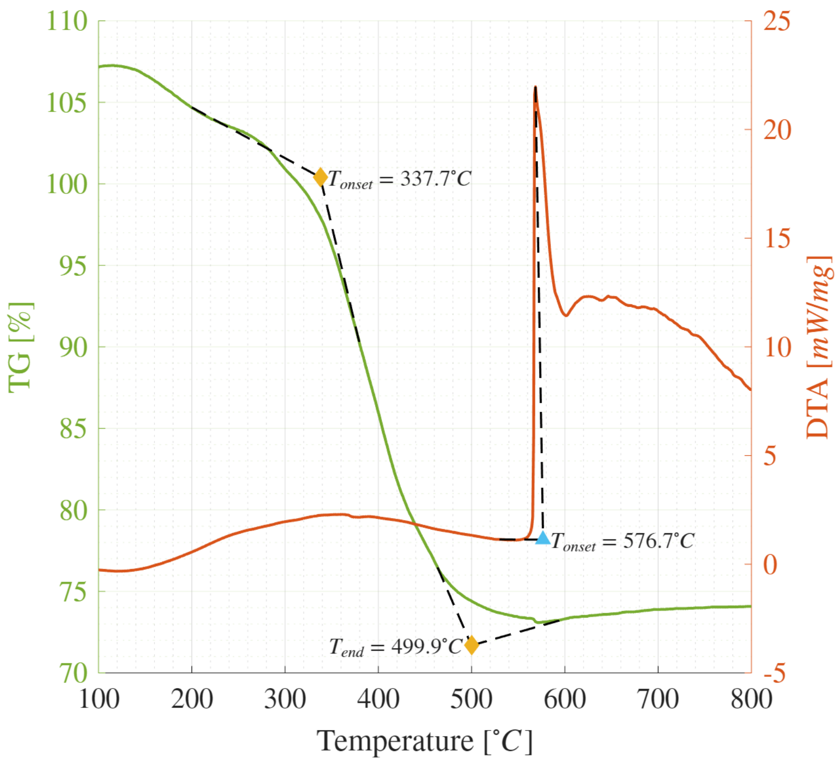

Figure 5: TG/DTA curves for the 60 % powder filler sample (bottom section)

reaction did not show a clear correlation with the loading, occurring at similar temperatures across different batches. Overall, the DTA onset temperature averaged 567.2 °C with a standard deviation of 21.1 °C, comparable to the variation within individual batches among the top, middle, and bottom sections. Therefore, the ignition temperature identified under DTA conditions can be considered independent from the powder fraction, as shown in Figure 6.

The thermogravimetric data were also used to estimate the actual powder fraction. Corrections for carbonaceous residues generated by the binder was introduced. Under similar test conditions, the resin High Speed 2.0 was found to leave about 14 % of residues, computed on the initial mass of the sample. While this provides an estimate of actual loading, the true binder fraction remains unknown. Results showed that the actual powder fraction approached the theoretical value for higher nominal loading, presenting also smaller deviations. This is likely due to increased viscosity at higher filler loadings reducing particle settling. Overall, samples exhibited near-nominal loading (Figure 7, with a mean deviation of (6.3 ± 1.7) % and (0.0 ± 0.7) % when corrected.

Table 4: Characteristic onset and end temperatures from thermogravimetric (TG) and differential thermal analysis (DTA). Temperature data are in °C

Sample	T_{onset} TG	T_{end} TG	T_{onset} DTA	Loading [% wt.]	Loading Corrected [% wt.]
60% Mg/SiO_2 loading					
60% TOP	337.7	499.9	576.7	65.5	59.9
60% MID	337.9	569.3	564.8	65.5	59.9
60% BOTTOM	331.9	488.4	532.7	64.2	58.6
Mean ± Std. Dev.	335.8 ± 3.4	519.2 ± 43.8	558.1 ± 22.8	65.1 ± 0.8	59.5 ± 0.8
50% Mg/SiO_2 loading					
50% TOP	331.9	488.4	591.1	58.5	51.5
50% MID	361.8	495.3	582.2	57.8	50.8
50% BOTTOM	353.4	495.9	555.5	56.2	49.2
Mean ± Std. Dev.	349.0 ± 15.4	493.2 ± 4.2	576.3 ± 18.5	57.5 ± 1.2	50.5 ± 1.2
40% Mg/SiO_2 loading					
40% TOP	356.8	476.1	N.D.	39.8	31.4
40% MID	346.3	487.2	560*	49.3	40.9
40% BOTTOM	353.8	486.7	560*	49.1	40.7
Mean ± Std. Dev.	352.3 ± 5.4	483.3 ± 6.3	560.0 ± 0.0‡	46.1 ± 5.4	37.7 ± 5.4

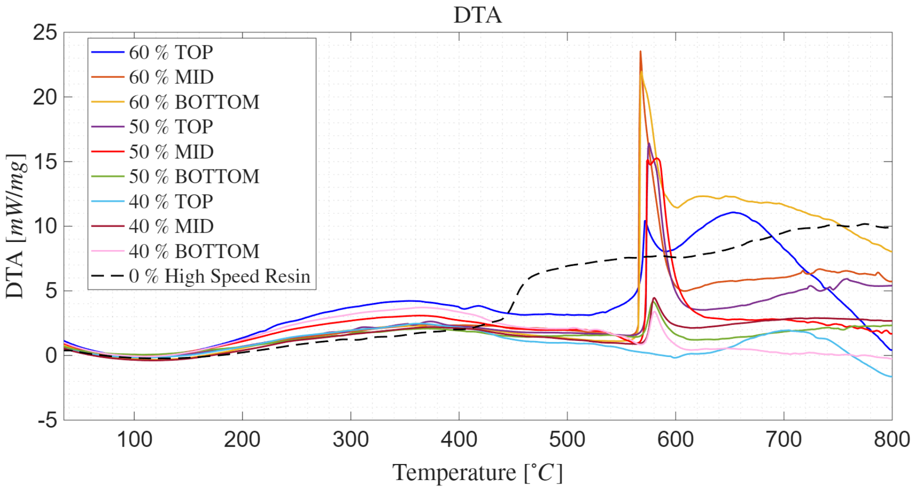

Figure 6: DTA diagnostics for samples with 40 %, 50 %, and 60 % loading, for top, mid, and bottom sections

4 Conclusions

This research demonstrated the possibility to manufacture thermite-loaded photocurable resins suitable for Digital Light Processing (DLP) additive manufacturing, and to use them for the production of samples. Composite resins with Mg/SiO_2 thermite powder loadings in excess of 60 % by mass were successfully printed. Repeatability of properties was demonstrates between batches. TG and DTA indicated that the pyrolysis onset temperature has a modest sensitivity to the powder loading, dropping slightly while pyrolysis end temperature rises. The onset of the exothermic thermite reaction appears unaffected by the

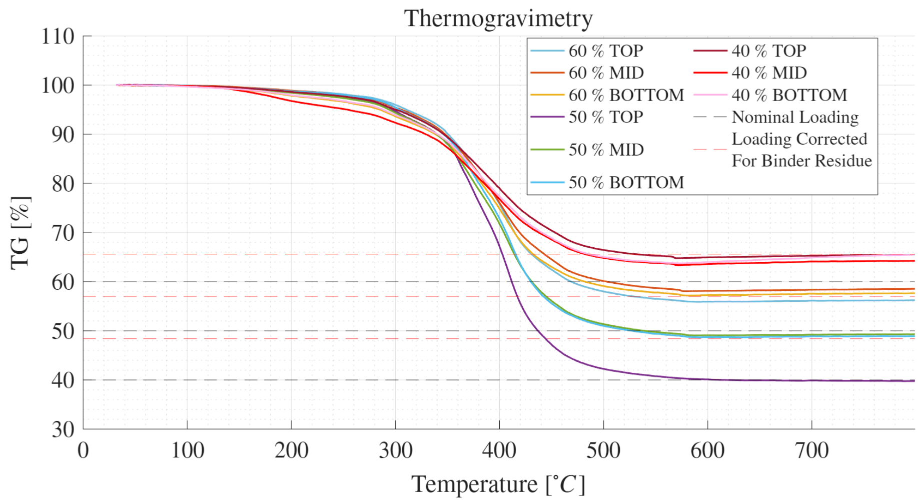

Figure 7: TG diagnostics for samples with 40 %, 50 %, and 60 % loading, for top, mid, and bottom sections

loading fraction, occurring once binder pyrolysis is completed. The estimated actual powder fractions, adjusted for residual carbonaceous binder content, indicated the fabricated samples are representative of nominal loading values, especially at higher powder loadings, where it is possible that viscosity decreases filler settling.

These results suggest that DLP printing of high-load thermite composites can be a viable pathway to manufacture energetic charges with complex shapes. This opens to the possibility of developing customized shapes, according to specific needs of integration. Said charges demonstrated a repeatable thermal behavior, fully dependent on thermite nature and, at least partially, on binder pyrolysis. Optimizing resin formulations and printing parameters remains crucial to further improve charge manufacturing quality and energetic output. Moreover, exploring novel powder formulations combined with mechanical activation techniques could provide a pathway to tailor the ignition temperature and overall reaction characteristics, potentially enhancing the performance and safety of Thermite-for-Demise (T4D) components. In this respect, non-spherical shape of activated particles may induce scattering and additional complexity in the printing process.

Future work should focus on evaluating the mechanical robustness, combustion performance, and behavior of the printed charges under conditions simulating satellite reentry. Additionally, investigations into the geometric precision of printed parts, the capability to produce custom shapes, and the potential for post-processing or machining of the components are necessary to fully assess the manufacturing approach. Finally, assessment of aging behavior in the space environment becomes crucial to understand if this solution can survive the space environment, from launch to satellite disposal maneuver.

5 Acknowledgement

The authors wish to express their sincere gratitude to Mr. Alberto Verga, Laboratory Manager of the Space Propulsion Laboratory at Politecnico di Milano, whose continuous support has been invaluable to

this work.
Funded by the European Union through the European Innovation Council (EIC) within the THREAD project (Grant agreement ID: 101186901). Views and opinions expressed are however those of the authors only and do not necessarily reflect those of the European Union or the European Innovation Council (EIC). Neither the European Union nor the granting authority can be held responsible for them.

European Innovation Council Funded by the European Union

References

AA.VV. ESA Space Debris Mitigation Requirements (ESSB-ST-U-007), Issue 1. ESA Standard document, October 2023. URL https://technology.esa.int/upload/media/ESA-Space-Debris-Mitigation-Requirements-ESSB-ST-U-007-Issue1.pdf.

AA.VV. Future of space economy. Technical report, McKinsey & Co., 2024.

AA.VV. Esa's annual space environment report. Technical report, European Space Agency, Space Debris Office, Robert-Bosch-Strasse 5, D-64293 Darmstadt, Germany, March 2025. Prepared by ESA Space Debris Office. Final release.

Anonymous. Creality HALOT-MAGE S 14K Resin 3D Printer, 2025. URL https://www.creality.com/products/creality-halot-mage-s. Accessed: 2025-04-30.

B. M. Cattani, A. Caiazzo, L. Innocenti, and S. Lemmens. An overview of design for demise technologies. In *Proceedings of the 8th European Conference on Space Debris, Darmstadt, Germany*, pages 20–23, 2021.

A. Finazzi, S. Carlotti, C. Paravan, F. Maggi, S. Dossi, T. Lips, D. Daub, T. Schleutker, G. Smet, and K. Bodjona. Thermite-for-demise (t4d): from material selection to test campaign. In *AIAA SciTech 2024 Forum*, page 2162, 2024a.

A. Finazzi, D. Daub, F. Maggi, C. Paravan, S. Dossi, T. Lips, G. Smet, and K. Bodjona. Thermite-for-demise (T4D): Experiments and numerical modelling on ball-bearing unit mock-ups containing thermite in an arc-heated wind tunnel. *Acta Astronautica*, 223:550–576, 2024b. doi: https://doi.org/10.1016/j.actaastro.2024.06.013.

A. Finazzi, P. Finocchi, S. Carlotti, and F. Maggi. Thermite-for-demise (t4d): Experimental analysis of heat transfer principles and preliminary sizing of an application. *International journal of heat and mass transfer*, 220:124957, 2024c.

S. Fischer and M. Grubelich. Theoretical energy release of thermites, intermetallics, and combustible metals. Technical report, Sandia National Lab.(SNL-NM), Albuquerque, NM (United States), 1998.

J. Foust. Propellant leak blamed for falcon 9 upper stage uncontrolled reentry, feb 2025. URL https://spacenews.com/propellant-leak-blamed-for-falcon-9-upper-stage-uncontrolled-reentry/.

X. Gao, J. Chen, X. Chen, W. Wang, Z. Li, and R. He. How to Improve the Curing Ability during the Vat Photopolymerization 3D Printing of Non-Oxide Ceramics: A Review. *Materials*, 17(11), 2024. ISSN 1996-1944. doi: 10.3390/ma17112626. URL https://www.mdpi.com/1996-1944/17/11/2626.

L. Guo, W. Song, M. Hu, C. Xie, and X. Chen. Preparation and reactivity of aluminum nanopowders coated by hydroxyl-terminated polybutadiene (htpb). *Applied Surface Science*, 254(8):2413–2417, 2008.

K. Kanishka and B. Acherjee. Revolutionizing manufacturing: A comprehensive overview of additive manufacturing processes, materials, developments, and challenges. *Journal of Manufacturing Processes*, 107:574–619, 2023. ISSN 1526-6125. doi: https://doi.org/10.1016/j.jmapro.2023.10.024. URL https://www.sciencedirect.com/science/article/pii/S1526612523009726.

T. Lips. Simulation of spacecraft destruction during atmospheric re-entry. ESA Academy – Space Debris Training Course 2025, Lecture slides, 2025. ESA Academy Training and Learning Programme.

Monique S. McClain, Aaron Afriat, Jeffrey F. Rhoads, Ibrahim Emre Gunduz, and Steven F. Son. Development and characterization of a photopolymeric binder for additively manufactured composite solid propellant using vibration assisted printing. *Propellants, Explosives, Pyrotechnics*, 45(6):853–863, 2020. doi: https://doi.org/10.1002/prep.201900387.

K.A. Monogarov, I.N. Melnikov, S.M. Drozdov, D. Dilhan, Yu.V. Frolov, N.V. Muravyev, and A.N. Pivkina. Pyrotechnic approach to space debris destruction: From thermal modeling to hypersonic wind tunnel tests. *Acta Astronautica*, 172:47–55, 2020. ISSN 0094-5765. doi: https://doi.org/10.1016/j.actaastro.2020.03.028. URL https://www.sciencedirect.com/science/article/pii/S0094576520301569.

S. Mueller, E. W. Llewellin, and H. M. Mader. The rheology of suspensions of solid particles. *Proceedings of the Royal Society A: Mathematical, Physical and Engineering Sciences*, 466(2116):1201–1228, 2010. doi: 10.1098/rspa.2009.0445.

R. Seiler and G. Smet. Exothermic reaction aided spacecraft demise during re-entry. Patent EP3604143A1, European Space Agency (ESA), 2020.

A. Smirnov, S. Chugunov, A. Kholodkova, M. Isachenkov, A. Tikhonov, O. Dubinin, and I. Shishkovsky. The fabrication and characterization of $BaTiO_3$ piezoceramics using sla 3d printing at 465 nm wavelength. *Materials*, 15(3), 2022. ISSN 1996-1944. doi: 10.3390/ma15030960. URL https://www.mdpi.com/1996-1944/15/3/960.

W. H. Strehlow and L. E. Cook. Compilation of energy band gaps in elemental and binary compound semiconductors and insulators. *American Chemical Society and the American Institute of Physics*, 1973.

P.M. Waswa and J.A. Hoffman. Illustrative NASA low earth orbit spacecraft subsystems design-for-demise trade-offs, analyses and limitations. *Int. J. Des. Eng.*, 5:21–40, 2012. doi: 10.1504/IJDE.2012.050280.